Research Article | Vol. 24, No. 18 | 5 Sep 2016 | OPTICS EXPRESS 19994

Optics EXPRESS

Femtosecond laser-induced hard X-ray generation in air from a solution flow of Au nano-sphere suspension using an automatic positioning system

WEI-HUNG HSU,[1] FRANCES CAMILLE P. MASIM,[1] MATTEO PORTA,[2] MAI THANH NGUYEN,[2] TETSU YONEZAWA,[2] ARMANDAS BALČYTIS,[3,4] XUEWEN WANG,[3] LORENZO ROSA,[3,5] SAULIUS JUODKAZIS,[3,6] AND KOJI HATANAKA[1,*]

[1]*Research Center for Applied Sciences, Academia Sinica, Taipei 115, Taiwan*
[2]*Division of Materials Science and Engineering, Faculty of Engineering, Hokkaido University, Hokkaido 060-8628, Japan*
[3]*Nanotechnology Facility, Center for Micro-Photonics, Swinburne University of Technology, Victoria 3122, Australia*
[4]*Institute of Physics, Center for Physical Sciences and Technology, Vilnius LT-02300, Lithuania*
[5]*Department of Information Engineering, University of Parma, Parma I-43124, Italy*
[6]*Melbourne Centre for Nanofabrication, the Victorian Node of the Australian National Fabrication Facility, Clayton 3168 Vic, Australia*
[*]*kojihtnk@gate.sinica.edu.tw*

Abstract: Femtosecond laser-induced hard X-ray generation in air from a 100-μm-thick solution film of distilled water or Au nano-sphere suspension was carried out by using a newly-developed automatic positioning system with 1-μm precision. By positioning the solution film for the highest X-ray intensity, the optimum position shifted upstream as the laser power increased due to breakdown. Optimized positioning allowed us to control X-ray intensity with high fidelity. X-ray generation from Au nano-sphere suspension and distilled water showed different power scaling. Linear and nonlinear absorption mechanism are analyzed together with numerical modeling of light delivery.

OCIS codes: (160.4236) Nanomaterials; (320.2250) Femtosecond phenomena; (320.7120) Ultrafast nonlinear phenomena; (340.0340) X-ray optics.

References and links

1. T. A. Labutin, V. N. Lednev, A. A. Ilyin, and A. M. Popov, "Femtosecond laser-induced breakdown spectroscopy," J. Anal. Spectrom. **31**, 90–118 (2016).
2. X. L. Liu, X. Lu, X. Liu, T. -T. Xi, F. Liu, J. -L. Ma, and J. Zhang, "Tightly focused femtosecond laser pulse in air: from filamentation to breakdown," Opt. Express **18**(25), 26007–26017 (2010).
3. E. G. Gamaly, "The physics of ultra-short laser interaction with solids at non-relativistic intensities," Phys. Rep. **508**, 91–243 (2011).
4. J. Passig, R. Irsig, N. X. Truong, T. Fennel, J. Tiggesbaumker, and K. H. Meiwes-Broer, "Nanoplasmonic electron acceleration in silver clusters studied by angular-resolved electron spectroscopy," N. J. Phys. **14**, 085020 (2012).
5. S. Mondal, I. Chakraborty, S. Ahmad, D. Carvalho, P. Singh, A. D. Lad, V. Narayanan, P. Ayyub, and R. Kumar, "Highly enhanced x-ray emission from oriented metal nanorod arrays excited by intense femtosecond laser pulses," Phys. Rev. B. **83**, 035408 (2011).
6. V. A. Andreeva, O. G. Kosareva, N. A. Panov, P. M. Solyankin, M. N. Esaulkov, P. Gonzalez de Martinez, A. P. Shkurinov, V. A. Makarov, L. Berge, and S. L. Chin, "Ultrabroad terahertz spectrum generation from an air-based filament plasma," Phys. Rev. Lett. **116**, 063902 (2016).
7. L. M. Chen, M. Kando, M. H. Xu, Y. T. Li, J. Koga, M. Chen, H. Xu, X. H. Yuan, Q. L. Dong, Z. M. Sheng, S. V. Bulanov, Y. Kato, J. Zhang, and T. Tajima, "Study of x-ray emission enhancement via a high-contrast femtosecond laser interacting with a solid foil," Phys. Rev. Lett. **100**, 045004 (2008).
8. K. Hatanaka, K. Yomogihita, H. Ono, K. Negafuchi, H. Fukumura, M. Fukushima, T. Hashimoto, S. Juodkazis, and H. Misawa, "Hard x-ray generation using femtosecond irradiation of PbO glass," J. Non-Crys. Sol. **354**, 5485–5490

#265200 http://dx.doi.org/10.1364/OE.24.019994
Journal © 2016 Received 13 May 2016; revised 15 Jul 2016; accepted 12 Aug 2016; published 22 Aug 2016

Optics EXPRESS

(2008).
9. K. Hatanaka and H. Fukumura, "Femtosecond laser-induced x-ray pulse emission from transparent materials including glasses," New Glass **19**, 61–66 (2008).
10. S. Kahaly, S. K. Yadav, W. M. Wang, S. Sengupta, Z. M. Sheng, A. Das, P. K. Kaw, and G. R. Kumar, "Near-complete absorption of intense, ultrashort laser light by sub-gratings," Phys. Rev. Lett. **101**, 145001 (2008).
11. S. Juodkazis, V. Mizeikis, S. Matsuo, K. Ueno, and H. Misawa, "Three-dimensional micro- and nano-structuring of materials by tightly focused laser radiation," Bull. Chem. Soc. Jpn. **81**, 411–448 (2008).
12. K. Hatanaka, T. Miura, and H. Fukumura, "Ultrafast x-ray pulse generation by focusing femtosecond infrared laser pulses onto aqueous solutions of alkali metal chloride," App. Phys. Lett. **80**(21), 3925 (2002).
13. K. Hatanaka, T. Miura, and H. Fukumura, "White x-ray pulse emission of alkali halide aqueous solutions irradiated by focused femtosecond laser pulses: a spectroscopic study on electron temperatures as functions of laser intensity, solute concentration and solute atomic number" Chem. Phys. **299**, 265–270 (2004).
14. K. Hatanaka, T. Ida, H. Ono, S. Matsushima, H. Fukumura, S. Juodkazis, and H. Misawa, "Chirp effect in hard x-ray generation from liquid target when irradiated by femtosecond pulses," Opt. Express **16**(17), 12650–12657 (2008).
15. D. Sato, S. Matsuhima, H. Ono, S. Kajimoto, H. Fukumura, and K. Hatanaka, "Circularly polarized femtosecond laser-induced pulsed x-ray emission from distilled water," Rev. Laser Eng. **37**(12), 101–104 (2009).
16. K. Hatanaka and H. Fukumura, "X-ray emission from CsCl aqueous solutions when irradiated by intense femtosecond laser pulses and its application to time-resolved XAFS measurement of I^- in aqueous solution," X-ray Spectrom. **41**, 195–200 (2012).
17. K. Hatanaka, T. Miura, H. Ono, and H. Fukumura, "Photon energy conversion of IR femtosecond laser pulses into x-ray pulse using electrolyte aqueous solutions in air," AIP Conf. Proc. **634**, 260–267 (2002).
18. K. Hatanaka, H. Ono, and H. Fukumura, "X-ray pulse emission from cesium chloride aqueous solutions when irradiated by double-pulsed femtosecond laser pulses," App. Phys. Lett. **93**, 064103 (2008).
19. A. E. Martirosyan, C. Altucci, A. Bruno, C. de Lisio, A. Porzio, and S. Solimeno, "Time evolution of plasma afterglow produced by femtosecond laser pulses," J. Appl. Phys. **96**(10), 5450–5455 (2004).
20. V .V. Bukin, N. S. Vorob'ev, S. V. Garnov, V. I. Lozovoi, A. A. Malyutin, M. Y. Schelev, and I. S. Yatskovskii "Formation and development dynamics of femtosecond laser microplasma in gases," Quan. Elec. **36**(7), 638–645 (2006).
21. S. Link and M. A. El-Sayed, " Spectral properties and relaxation dynamics at surface plasmon electronic oscillation in gold and silver nanodots and nanorods," J. Phys. Chem. B **13**, 8410–8426 (1999).
22. L. Delfour and T. E. Itina, "Mechanisms of ultrashort laser-induced fragmentation of metal nanoparticles in liquids: numerical insights," J. Phys. Chem. C. **119**, 13893–13900 (2015).
23. D. Bauer, T. Brabec, H. Fehske, S. Lochbrunner, K. H. Meiwes-Broer, and R. Redmer, "Focus on correlation effects in radiation fields," N. J. Phys. **15**, 065015 (2013).
24. P. Wopper, P. M. Dinh, P. -G. Reinhard, and E. Suraud, "Electrons as probes of dynamics in molecules and clusters: a contribution from time dependent density functional theory," Phys. Rep. **562**, 1–68 (2015).
25. K. Hatanaka, M. Porta, F. C. P. Masim, W. -H. Hsu, M. T. Nguyen. T. Yonezawa, A. Balčytis, and S. Juodkazis, "Efficient x-ray generation from gold nano-colloidal suspensions," Sci. Rep. (in review; available as arXiv preprint http://arxiv.org/abs/1604.07541) (2016).
26. M. Kondoh and M. Tsubouchi, "Liquid-sheet jets for terahertz spectroscopy," Opt. Express **22**, 14135–14147 (2014).
27. Y. J. Choo and B. S. Kang, "Parametric study on impinging-jet liquid sheet thickness distribution using an interferometric method," Exp. Fluids **31**, 56–62 (2001).
28. F. C. P. Masim, H. L. Liu, M. Porta, T. Yonezawa, A. Balčytis, S. Juodkazis, W. H. Hsu, and K. Hatanaka, "Enhanced photoacoustics from gold nano-colloidal suspensions under femtosecond laser excitation," Opt. Express **24**(13), 14781–14792 (2016).
29. F. C. P. Masim, W. H. Hsu, C. -H. Tsai, H. L. Liu, M. Porta, M. T. Nguyen, T. Yonezawa, A. Balčytis, X. Wang, S. Juodkazis, and K. Hatanaka, "MHz-ultrasound generation by chirped femtosecond laser pulses from gold nano-colloidal suspensions," Opt. Express **24**(14), 17050–17059 (2016).
30. N. Linz, "Wavelength dependence of nanosecond infrared laser-induced breakdown in water: Evidence for multiphoton initiation via an intermediate state," Phys. Rev. B. **91**, 134114 (2015).
31. H. Wang, K. Wang, J. Liu, H. Dai, and Z. Yang, "Theoretical research on terahertz air-breakdown coherent detection with the transient photocurrent model," Phys. Rev. B. **20**, 19264 (2012).
32. V. Mizeikis, E. Kowalska, and S. Juodkazis, "Resonant localization, enhancement and polarization of optical fields in nano-scale interface regions for photocatalytic applications," J. Nanosci. Nanotechnol. **11**, 2814–2822 (2011).
33. R. Menzel, *Photonics: Linear and Nonlinear Interactions of Laser Light and Matter*, (Springer, 2001).

1. Introduction

Intense femtosecond laser interaction with condensed matters involves linear and nonlinear absorption [1], which usually results in plasma formation [2], ablation [3], electron emission [4], X-ray [5], and THz wave [6] generation. The interaction of ultra-short laser pulses and matter results in laser-induced breakdown through optical absorption. It is accompanied by the formation

Optics EXPRESS

of localized highly ionized plasma with a typical density of hundreds-of-molecules in the focal region of a laser beam [2]. Solid density plasma leads to the design of novel micrometer-sized X-ray, THz, electron and ion sources [5]. The highly progressive development of compact and efficient X-ray and THz sources demonstrated great contributions in biological and medical fields [4–6].

Recent advances in practical X-ray sources based on laser-induced breakdown are beneficial for probing ultrafast real-time dynamics of physical and chemical systems for micro-scale imaging [5]. Solid targets such as metals [7] and transparent glasses [8, 9] with flat surfaces have been used for X-ray generation under intense femtosecond laser irradiation. Other attempts to enhance X-ray intensity by the design of structured [10] and layered [11] surfaces as targets have been successfully carried out. The enhancement of X-ray intensity is attributed to effective increase of absorption efficiency, surface plasmon resonance effects and enhanced generation of high-energy electrons from highly ionized plasma.

On the other hand, liquid targets for femtosecond laser-induced X-ray generation have attracted attention due to the possibility to control the X-ray spectra via choices of solute contents of the micro-jet [12]. Recent experimental studies on liquid targets were extensively carried out by Hatanaka, et al., which showed various aspects of femtosecond laser-induced X-ray generation using alkali halide aqueous solutions such as CsCl and RbCl [12–18] from the viewpoints of electron temperature dependent on laser intensity, solute concentration, and solute species [13], X-ray emission efficiency as a function of the laser chirp (pulse width) [14], and extraordinal enhancements of X-ray intensity under the double pulse excitation [18]. Since liquid targets can be recycled and circulated by a pump, it is considered to be durable for long-time X-ray generation. This is advantageous for time-resolved measurements such as X-ray absorption spectrosopy [16] wherein long-time accumulation is indispensable. One possible disadvantage for liquid targets is that X-ray generation experiments should be performed under atmospheric pressure, not in vacuum chambers. When femtosecond laser pulses were tightly-focused in air, the formation of high density plasma is inevitable [19, 20].

Plasmonic metal nanoparticles are of great importance, primarily due to their biocompatibility, superior optical properties, large absorption cross section and spectral selectivity based on surface plasmon resonance [21]. Femtosecond laser-irradiation to nanoparticles and nanoclusters leads to the subsequent conversion of absorbed energy into energetic ions, electrons, and X-rays [22–24]. Nanoparticle-facilitated absorption of femtosecond laser pulses is relevant for wider fields of applications ranging from pulsed X-ray generation to energetic particle sources [4]. Surface plasmon resonant excitation in nanoparticles is crucial for the efficient absorption and generation of extreme atomic charge states [23, 24]. Efficient X-ray generation from Au nano-colloidal suspensions under intense femtosecond laser irradiation has been demonstrated with different particle sizes of gold nanoparticles [25].

Since air plasma formation is inevitable under atmospheric pressure for X-ray generation from liquid targets, fine tuning and control for optimization is necessary. In this paper, an automatic positioning system was designed to optimize the position of liquid thin film target solution to reach the highest X-ray intensity emission under femtosecond laser excitation. Au nano-sphere colloidal suspension was used to enhance the X-ray emission intensity.

2. Experiments

An automatic positioning system was designed for the optimization of X-ray emission by changing the position of solution film surface to the laser focus. The experimental setup is shown in Fig. 1. Two glass pipette nozzles (inner diameter = 1 mm), which are attached to a circulation pump (PMD-211, SANSO), make two colliding solution flows. Such collision results in the formation of thin solution film as described elsewhere [26, 27]. The solution film is oriented vertically to the solution flows from the nozzles. The estimated thickness of the solution film is $\sim 100\ \mu$m.

Optics EXPRESS

The surface of the solution film is perfectly smooth without any turbulence as shown in the inset of Fig. 1. The glass nozzle holders were mounted to a 3D-automatic (KS701-20LMS, SURUGA SEIKI) and rotation stages (KS401-60, SURUGA SEIKI), so that the position and the angle of the solution film can be mechanically controlled.

Chirp-free femtosecond laser pulses (40 fs, 800 nm, 1 kHz, horizontally-polarized, Mantis, Legend, Elite, HE USP, Coherent, Inc.) are tightly focused in air with an off-axis parabolic mirror (the effective focus length = 50.8 mm, the reflection angle = 90 degrees, and the numerical aperture NA = 0.25), 47-097, Edmund Optics) onto the solution film as shown in the inset. The laser power was in between 0.1 W and 1 W by adjusting a half-wave plate (65-906, Edmund Optics) and a polarization beam splitter (47-048, Edmund Optics), which are inserted into the optical path right after the regenerative amplifier before the compressor in the laser system. The local laser power after being focused tightly to the solution film surface was estimated to be $\sim 1.41 \times 10^{14}$ W/cm^2 when the laser power was 1 W by considering the effective focus size (as shown later in Fig. 3). The incident angle of the laser pulse was at 60 degrees to the normal of the solution film. The solution flow rate is approximately 180 mL/min, while the laser pulse width, the focus size, and the repetition rate are 40 fs, a few tens of $\sim \mu$m, and 1 kHz, respectively. Therefore, every single laser pulse irradiates the fresh surface of the solution film. A Geiger counter (SS315, Southern Scientific) was used for X-ray measurement. The major gas component of the Geiger counter is helium (> 95%, ~0.5 bar) with some halogens as quenching agent. The input window material is mica (1.6 - 2 mg/cm^2) and its thickness is ~6μm. The distance between the laser focus (the X-ray point source) and the Geiger counter was 15 cm. For X-ray photon counting measurements considering the pile-up effects, the Geiger counter head was covered by an aluminum-made iris with a 1-mm hole. All the experiments in this paper were carried out in air under atmospheric pressure (1 atm) at room temperature (296 K). Therefore, it is sure that the Geiger counter detects X-ray, not α-ray or β-ray.

A LabView (2013, National Instruments, Inc.)-based code for this experiment controls the x-axis position of the automatic stage continuously for the X-ray count to be the highest. The spatial resolution of the 3D-automatic stage is 1 μm and the backlash is less than 0.5 μm. The time sequence and position-dependent X-ray intensity are shown in Fig. 2, where the sample solution is a distilled water and the laser power is 1 W. First, the code sets the scan velocity at 300 μm/sec then the stage starts moving fast with set velocity. Once the counter measures more than 5 counts/sec, the stage immediately decreases its velocity to 1 μ/sec, then the code tries to find out the real peak position in the region ±10 μm around the tentative peak position. During this process, the X-ray intensity may decrease when the stage leaves away from the real peak position, then the code sets other velocities at 5 and 40 μm/sec in the regions ±50 μm and ±375 μm around the real peak position, respectively. The code sets a threshold value for X-ray count at 5% of the peak count. When the counter measures lower than the threshold, the stage changes its moving direction from forward to backward, and vice versa. This is the reason why the system loses the X-ray emission during the stage movements as indicated by blue and green arrows in Fig. 2. However, since the scan velocities at the regions far away from the peak position are set very high, the system immediately re-optimizes the position for X-ray emission. The threshold was set intentionally at 5% to take the whole envelope of the X-ray emission as a function of the solution position. For practical applications of X-ray, the threshold can be set on demand, at 90% for instance.

A solution of Au nano-sphere colloidal suspension with an absorption peak at 520 nm (diameter of $2r$ = 20 nm) was prepared via a citrate reduction synthesis method as described elsewhere [28, 29]. Atomic concentration of $\sim 1.4 \times 10^{-4}$ mol/L and particle concentration of $\sim 4.21 \times 10^{18}$ NPs/mL of Au nano-colloidal suspension was used for X-ray generation experiments. Its absorption spectrum (not shown) was typical for a mono-dispersed solution of nanoparticles.

Optics EXPRESS

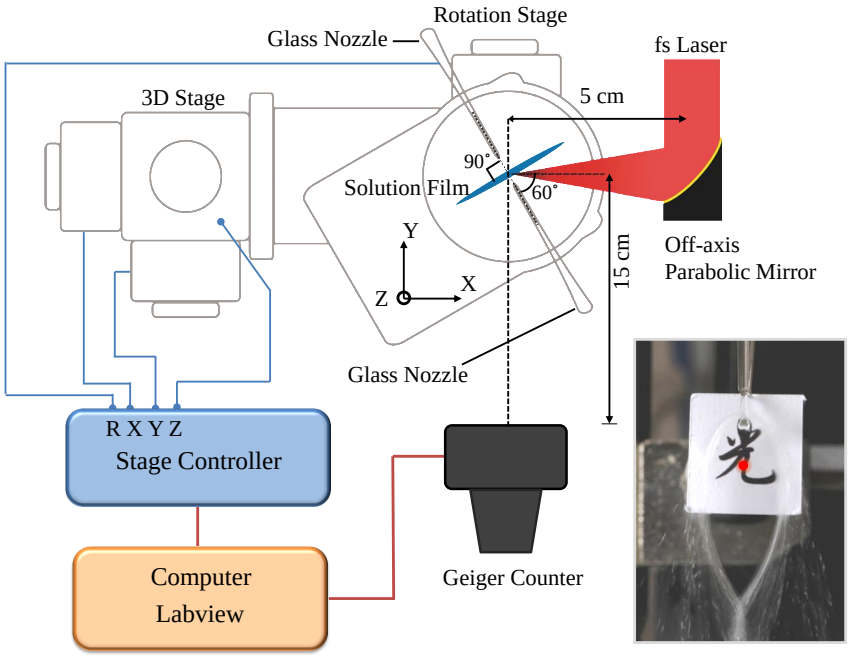

Fig. 1. Experimental set-up of the automatic positioning system for X-ray emission from solutions. Angle of incidence $\theta = 60°$. Laser pulses of $\lambda = 800$ nm wavelength and $t_p = 40$ fs were used in experiments at 1 kHz repetition rate. The red mark in the inset photo indicates the position of the laser focus.

3. Results and discussion

3.1. X-ray generation from distilled water

Fig. 3(a) shows position-dependent X-ray intensities as the laser power increased from 0.1 W to 1 W, the optimum position of the solution film surface shifted ~ 50 μm. Similarly, the laser focus point shifted toward the laser source as indicated in Fig. 3(b) which is captured by a CCD (DMK23U274, Imaging Source) with an objective lens (M Plan Apo 5x, Mitutoyo). Focusing with a parabolic mirror of numerical aperture NA = 0.25 would create a focus of $2w_0 = 4$ μm diameter for an aberration-free performance without nonlinear effects. The corresponding axial extent of the focus approximated as two Rayleigh lengths is $2z_R = \pi w_0^2/\lambda \simeq 16$ μm. The side view images of the air breakdown region (no film) at different laser powers are shown in Fig. 3(b). The threshold values of the laser power to induce air breakdown have been reported to be about 2 - 4×10^{14} W/cm^2 when the laser pulse width is between 60 fs and 130 fs [1, 2, 19, 20]. The region at the very threshold of air breakdown ($P_a = 0.1$ W) shows length of ~ 50 μm and up to 0.4 mm at the highest power, 1 W. Importantly, there was no strong shift of the breakdown region from the initial position observed at low power (location of the film in X-ray generation experiment). Some upstream shift of the focal region is due to interplay between instantaneous reflectivity due to Kerr effect - an increase of the refractive index (Sec. 3.2), plasma formation due to ionization, and self-focusing. This shows that light delivery on the film is possible, however, should be optimized for the strongest interaction.

Steering of laser focus onto the film showed a very strong sensitivity for the misplacement along the direction of light propagation [Fig. 2(a)]. Only at optimum position, the largest reading

Optics EXPRESS

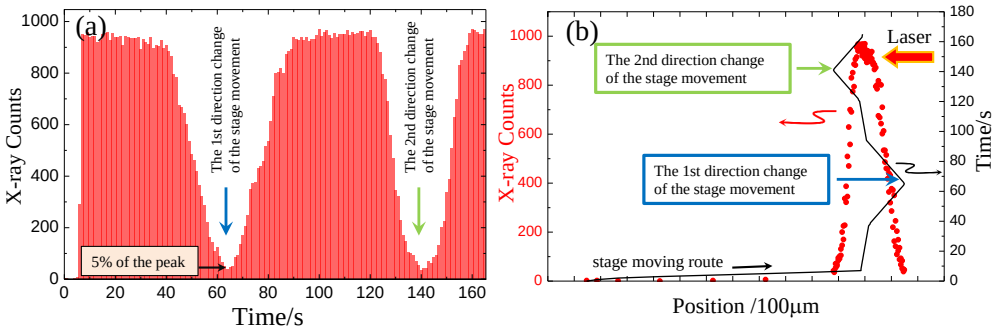

Fig. 2. Time sequence of X-ray counts (a) and position-dependent X-ray counts (red circle) (b) measured with a Geiger counter when the laser power P_a was 1 W. X-ray intensities at the valleys pointed by the green and blue arrows are lower than 5% of the peak intensity (a), where the 3D-automatic stage changed its moving direction. The black line (b) which indicates the moving route of the 3D-automatic stage shows its moving direction change pointed by the blue and green arrows as in (a). Additionally, the slope of black line shows that the 3D-stage moved with a starting velocity of 300 μm/sec to find out the peak position quickly; furthermore, while approaching the peak position, the 3D-automatic stage decreased its velocity to 1 μm/sec to recognize the peak finely.

of Geiger counts was obtained. For the $P_a = 0.1$ W average power the full width at half maximum (FWHM) was ~ 35 μm while for 1 W ~ 150 μm, which was almost a linear scaling closely following expected geometry of the breakdown region observed in air [Fig. 3(b)]. Time series of counts during the beam placement optimization reveals that a stable high intensity X-ray emission can be obtained and maintained [Fig. 2(a)]. This can be also used to achieve a tunability of X-ray intensity since changing laser power can slightly affect pulse duration and spectrum [25]

The case of light-matter interaction for X-ray generation by ultra-short laser pulses is a strongly nonlinear phenomenon. However, to understand peculiarities of complex simultaneously occurring and competing energy absorption and dissipation processes over long time scales and to optimize light delivery on the target, a linear performance of optical setup should be understood first [30–32]. Fig. 3(c) shows a numerical simulation of light intensity on the film at generic conditions of X-ray generation experiments without complications of nonlinear light-matter interaction. Positioning of laser beam onto a front surface of film was used in experiments.

3.2. *From nonlinear to linear X-ray generation: Au nano-sphere suspensions*

Light-matter interaction can be phenomenologically described by light-induced polarization, $\mathbf{P}$, which is expressed as additive orders. The first order term describe linear material response while the higher-orders define nonlinear light-matter interactions. The third order effects have the strongest nonlinear light-matter contribution in an isotropic medium where the second order effects are absent $\mathbf{P^{(2)}} = 0$ due to symmetry rules. The first relevant nonlinear term is $\mathbf{P}^{(3)} = \varepsilon_0 \chi^{(3)} \mathbf{E_1 E_2 E_3}$, where $\chi^{(3)}$ is the third-order nonlinear susceptibility (a four-dimensional tensor), ε_0 is susceptibility of vacuum, and $\mathbf{E_1}, \mathbf{E_2}, \mathbf{E_3}$ are the incident field vectors. The cumbersome expression of $\mathbf{P}^{(3)}$ is simplified in particular geometries and especially in the case of isotropic materials considered here: $P_m^{(3)} = \varepsilon_0 e_{11} E_m (\mathbf{EE})$ with $m = x, y, z$ and e_{11} denoting an element of $\chi^{(3)}$ [33]. The nonlinear refractive index dependent on intensity $I \sim E^2$ is given

Optics EXPRESS

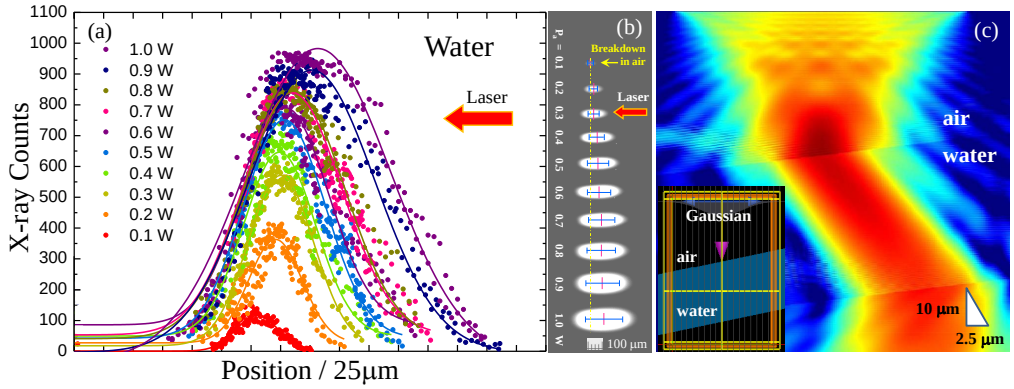

Fig. 3. X-ray intensity spatial profile (a), air plasma (b) as a function of laser power, and (c) numerical simulation of light focusing on a water jet at the used experimental conditions. Focal position in air would be in the middle point of the jet. Inset shows a setting for FDTD simulations (Lumerical). Intensity is plotted in logarithmic scale from -3 to -0.18 for the linearly p-polarized Gaussian beam of intensity $E^2 = 1$.

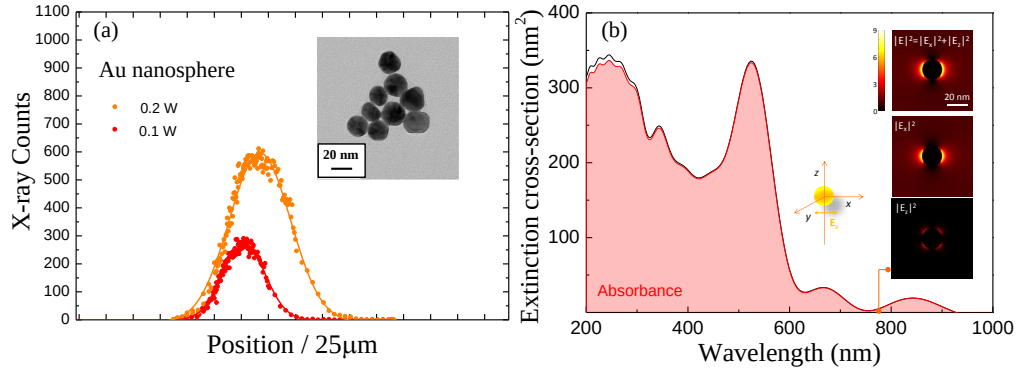

Fig. 4. X-ray intensity from Au nano-sphere colloidal suspension at 0.1 and 0.2 W laser power (a). Inset shows TEM image of Au spherical particles with a diameter of 20 nm. (b) FDTD calculated (Lumerical) extinction cross-section spectrum of $2r = 20$ nm diameter gold nanoparticles suspended in an aqueous refractive index environment, normalized to the geometric footprint area of the particle. Shaded area indicates the overwhelming dominance of absorption in the total extinction. Inset shows the total electric field intensity distribution in the xz plane as well as its constituent $|E_x|^2$ and $|E_z|^2$ projections at the excitation wavelength $\lambda = 800$ nm (b).

by [33]:

$$n(I) = n_0 + \frac{1}{2} e_{11} c_0 \varepsilon_0 E^2 \equiv n_0 + \gamma(\nu_{inc}) I, \tag{1}$$

where n_0 is the unperturbed refractive index, c_0 is the vacuum speed of light, and the coefficient $\gamma(\nu_{inc})$ is dependent on the frequency of incident field ν_{inc} and polarization: $\gamma^{lin} = \frac{3}{8}\frac{e_{11}}{n_0}$ and $\gamma^{cir} = \frac{1}{8}\frac{e_{11}}{n_0}$ for the linear and circular polarizations, respectively. The nonlinear refractive index, a $\chi^{(3)}$ Kerr-effect, which is related to the real part of dielectric function of material and describes

Optics EXPRESS

dispersive instantaneous material response, is polarization sensitive. For example, a circularly polarized light experiences lesser self-focusing due to smaller γ^{cir} factor as compared with linear polarization. Future experiments on X-ray generation will explore opportunities of polarization control. It is expected that for water where nonlinear mechanism of X-ray generation occurs, strong Kerr contribution and self-focusing can be used to enhance X-ray emission. Also, angular orientation of film is another polarization sensitive attribute to explore.

Fig. 4(a) shows the experimental results with Au nano-sphere suspensions when the laser power was set to 0.1 and 0.2 W. As shown in the inset, the diameter of Au particle is 20 nm. Similar results as distilled water were obtained. A linear scaling can be inferred from the Geiger counts at lowest laser power while for the water it is nonlinear. This is understandable due to a direct absorption of gold nanoparticles, which is linear while in water the breakdown is initiated via nonlinear multi-photon process.

Small metallic nano-particles almost do not scatter light and their extinction (optical loss measured in transmission) is solely defined by absorption cross section $\sigma_e \equiv \sigma_s + \sigma_a \simeq \sigma_a$ as shown by numerical simulations in Fig. 4(b). Finite different time domain (FDTD) method was used to reveal extinction spectrum and light localization relevant for the experiments with 20-nm-diameter Au nanoparticles in water. The wavelength of plasmonic resonance of gold at $\sim$ 520 nm could be targeted to enhance absorption, hence, X-ray emission. The insets in Fig. 4(b) show light localization with up to 9 times higher intensity at the interface with water even for the used 20 nm nanoparticles with a comparatively low extinction. The linear absorption properties of nanoparticles together with linear and nonlinear light propagation described above are essential to define the initial light delivery onto nanoparticle jet solution. X-ray generation from liquid targets pre-dominantly occurrs via the resonant absorption at the conditions of multi-photon absorption and avalanche ionization [14].

4. Conclusions and outlook

A 4-D (x, y, z, and rotation) fine positioning system with 1-μm precision for solution films was developed and applied for femtosecond laser-induced hard X-ray generation in air from distilled water and a gold nano-sphere (20 nm in diameter) suspension. A Labview-based code enabled us to find optimum positions of solution film surface to the laser focus automatically. The optimum positions shifted toward the direction of the laser source when the laser power increased. This shift can be attributed to laser-induced air-plasma formation and imaging experiments. Experimental results with a gold nano-sphere suspension indicate a slightly different X-ray emission from the case of distilled water attributed to different mechanisms of the laser pulse absorption. This prototype system is promising for the investigation of X-ray generation in air from various solutions as well as potential applications of hard X-ray source for imaging.

Funding

SJ is grateful for partial support via the Australian Research Council DP130101205 Discovery project and by the nanotechnology ambassador fellowship program at the Melbourne Centre for Nanofabrication (MCN) in the Victorian Node of the Australian National Fabrication Facility (ANFF).

Acknowledgment

TY acknowledges the partial support of Murata Foundation.